OPEN

Correspondence and
requests for materials
should be addressed to
M.F.G.-P. (maria.
garcia-parajo@icfo.es)

PSF decomposition of nanoscopy images via Bayesian analysis unravels distinct molecular organization of the cell membrane

Carlo Manzo[1], Thomas S. van Zanten[1], Suvrajit Saha[2], Juan A. Torreno-Pina[1], Satyajit Mayor[2] & Maria F. Garcia-Parajo[1,3]

[1]ICFO-Institut de Ciències Fotòniques, Mediterranean Technology Park, 08860 Castelldefels (Barcelona), Spain, [2]National Centre for Biological Sciences (TIFR), Bellary Road, Bangalore 560065, India, [3]ICREA-Institució Catalana de Recerca i Estudis Avançats, 08010 Barcelona, Spain.

The spatial organization of membrane receptors at the nanoscale has major implications in cellular function and signaling. The advent of super-resolution techniques has greatly contributed to our understanding of the cellular membrane. Yet, despite the increased resolution, unbiased quantification of highly dense features, such as molecular aggregates, remains challenging. Here we describe an algorithm based on Bayesian inference of the marker intensity distribution that improves the determination of molecular positions inside dense nanometer-scale molecular aggregates. We tested the performance of the method on synthetic images representing a broad range of experimental conditions, demonstrating its wide applicability. We further applied this approach to STED images of GPI-anchored and model transmembrane proteins expressed in mammalian cells. The analysis revealed subtle differences in the organization of these receptors, emphasizing the role of cortical actin in the compartmentalization of the cell membrane.

T he plasma membrane of eukaryotic cells is a receptor-rich lipid bilayer that mediates essential cell functions. In the presence of appropriate stimuli, membrane receptors may undergo interactions with other proteins, membrane lipids, ligands and/or the actin cytoskeleton, which are reflected in changes of their nanoscale spatial rearrangement[1–3]. In this scenario, quantitatively underpinning the molecular organization of receptors on the cell membrane is crucial to unravel the mechanisms used by the cellular machinery to accomplish efficient signaling. Such task requires the use of techniques suitable for nanoscale interrogation as well as robust analytical tools for quantification.

Recently, optical super-resolution techniques (STORM, PALM, f-PALM, STED, NSOM)[4–9] have been successfully exploited to visualize the nanoscale (co)-organization of different receptor proteins[10–15]. Unfortunately, several factors impose major challenges for reliable quantification of molecular positions and cluster stoichiometry even at sub-diffraction resolution. Besides effects related to antibody-labeling procedures (use of primary-secondary antibodies, variance in the number of fluorophores per antibody) and inherent fluorescent probe photo-physics (stochastic nature of photoswitching, occurrence of multiple-reactivation events, limited photo-activation efficiency and/or photobleaching) a major limiting factor for image quantification is represented by the high (local) molecular density in relation with the imaging resolution. Indeed, light diffraction imposes an upper limit to the density for resolving single fluorescent objects. This density is such that the number of labeled molecules within the area of an Airy disk must be of the order of unity. This limitation is even more stringent when automated localization algorithms are applied to fit images by means of a model point–spread function (PSF). For conventional fluorescence microscopy (FWHM $\sim$ 300 nm), the maximum resolvable density is $\rho \leq 1\ \mu m^{-2}$ [16]. Localizations techniques like STORM, PALM and f-PALM circumvent this limitation by stochastically tuning the density of simultaneously fluorescent molecules by photoactivation[4–6]. Yet, obtaining a low effective density in each sequential frame requires the use of high laser powers and long acquisition times. Recently, several computational methods have been developed to improve localization efficiency of overlapping PSFs at higher densities, thus reducing image acquisition time and limiting photobleaching effects related to high power and

long imaging cycles. These methods rely on multi-PSF fitting of the image intensity map and have shown excellent results, with 50% recall[17] (i.e., the percentage of identified molecules over the total number of molecules) at $\rho \sim 10$ μm^{-2} [16,18–23]. Other super-resolution methods, such as STED[7,8] and NSOM[9], shrink the width of the PSF (FWHM = 30–90 nm) as compared to conventional microscopy. In both cases, images are obtained at full labeling density, without the possibility of tuning the molecular density by stochastic photoactivation. Therefore, at densities corresponding to typical membrane-receptor expression levels ($\rho \sim 200$ μm^{-2}) a 30-nm resolution in combination with multi-PSF fitting algorithm would result in a recall ≤20%[16]. In addition, heterogeneity in receptor distribution can locally produce large density fluctuations, further impacting the recall rate. As a consequence, even at the superior resolution offered by STED and NSOM, it is challenging to fully determine molecular localization positions from dense samples. In this scenario, better algorithms capable of improving fitting in high-density regions would not only improve imaging speed for localization microscopy, but will also allow extracting particle localizations from STED and NSOM images, allowing accurate quantification of molecular organization at the nanoscale.

Here we present an approach that relies on the use of Bayesian inference to determine molecular localizations in dense samples. The method takes advantage of a likelihood-based hierarchical routine that sequentially classifies the region of interest and an intensity-based determination of the number of PSFs. In this way a high recall rate for closely spaced molecules even at moderate super-resolution conditions can be achieved while maintaining a low false-positive detection rate. The algorithm performance was tested on synthetic images in a wide range of experimental conditions. Application of the algorithm to STED images of glycosylphosphatidyl inositol-anchored proteins (GPI-AP) and model transmembrane receptors allowed quantification of protein spatial organization and revealed the influence of actin cytoskeleton on their inhomogeneous distribution.

Results

Algorithm description. We developed an algorithm combining hierarchical sub-region selection and marker-intensity Bayesian inference to improve particle localization from dense fluorescence images. The method only requires two input parameters: the width of the PSF and the intensity distribution of individual receptor markers. Both quantities can be evaluated from images of sparse immobilized fluorescent markers on glass or on the cell membrane (see Supplementary Fig. S1 online). The image is reconstructed as a sum of PSFs whose individual peak intensities are drawn according to the experimental distribution of single markers. The different blocks of the algorithm are assembled in an iterative loop that progressively builds up a reconstructed image while correspondingly deflating the raw image (REC/SUB block). A schematic view of the algorithm implementation and its flow diagram are depicted in Fig. 1. A detailed description is provided in Supplementary Methods and Fig. S2 online.

In order to limit computational complexity, PSF multi-fitting is generally performed sequentially in selected sub-regions of the full image. The choice and the order of the sub-regions to be analyzed are crucial for optimum particle localization. In the presence of heterogeneous signals and large fluorescence features, a threshold-based sub-region extraction from the filtered image might impact on the recall and false positive identification. Therefore, we developed a hierarchical sub-region selection routine based on the likelihood function evaluation (SEARCH). The routine does not require image preprocessing or thresholding. Specifically, the routine uses fast Fourier transform analysis to transform the image in a likelihood map, in which each pixel has a value corresponding to the likelihood for having Poisson noise in the surrounding box (see Supplementary

Methods and Fig. S2 online). The minimum pixel value thus corresponds to the center of the region containing higher fluorescence intensity variability. This evaluation establishes an objective criterion for sub-region classification. In addition, in the presence of intense fluorescence patches such as large receptor clusters, the SEARCH routine first pinpoints the areas at the border of the patch where the maximum information is contained. Successive fitting and deflation steps allow to progressively eroding the patch towards the center. Once the SEARCH routine has pinpointed the sub-region most-likely candidate to contain markers, the algorithm proceeds to its further analysis, attempting to reconstruct it via the fitting routine box-BIC. This is achieved via modeling the box intensity profile as a sum of n bi-dimensional Gaussian functions, approximating the instrumental PSF[24]. For each box, several models (n = 1,…,n$_{max}$) are evaluated by the minimization of the Bayesian Information Criterion (BIC)[25]:

$$BIC(n) = -2\log\left(\prod_{i,j=1}^{b_w} L_{rec}(I_{i,j}) \prod_{k=1}^{n} L_{int}(I_k)\right) + 3n, \qquad (1)$$

where the first product in the logarithm represents the goodness of the model in reconstructing the image, and the second term corresponds to the likelihood for the PSF peak intensities to belong to the marker intensity distribution. The last term introduces a penalty for the addition of further PSFs preventing overestimation of the particle number. PSF center positions and intensity are used as free parameters in the optimization. The number of PSFs in the model (n) is iteratively increased until a stable global minimum of the BIC is obtained. The PSFs corresponding to the best model are then subtracted from the raw image (REC/SUB) and the analysis is iterated recursively[26] on the resulting image. At each iteration the global likelihood of the subtracted image intensity is evaluated and the algorithm is stopped when further subtraction of PSFs does not cause an increase in the likelihood value. Although this choice allows fast calculation, it tends to overestimate the number of emitters and to produce a high false positive recognition rate. Therefore, the routine is finally refined by the cumulative BIC analysis on the entire reconstructed image. In this final step, all the individual localizations previously retrieved are sorted in descending order of their individual likelihood and the BIC is cumulatively calculated over the whole image. The localizations producing a decrease of the overall BIC up to a global minimum are retained, whereas those producing a BIC increase are excluded (see Supplementary Methods and Fig. S2 online).

Evaluation of algorithm performance. Besides molecular density, other factors such as the width of the PSF, background noise and marker brightness distribution significantly affect particle localization accuracy. While PSF width and noise depends on instrumental settings, marker brightness distribution is related to the labeling marker. For STED and NSOM microscopy, receptors are typically labeled with antibodies containing one or more organic fluorophores[13–15,27]. The brightness intensity distribution (see Supplementary Fig. S1) accounts for the fluorophore quantum yield, mean and variance of the number of fluorophores per antibody and the intrinsic stochasticity of fluorophore emission. Since our algorithm takes advantage of such a distribution to infer on particle localization, we also sought to evaluate its impact on the algorithm performance. Therefore, we generated synthetic images at different molecular densities while varying the full-width-at-half-maximum (FWHM) of the PSF, signal-to-noise ratio (SNR, calculated as 20 times the logarithm of the mean brightness over the background noise standard deviation), average intensity (I) and width (σ_I^2) of the marker brightness distribution. The analysis of simulated data (Fig. 2) shows the algorithm capability to reconstruct raw images in a wide range of molecular densities (up to 200 μm^{-2}) at moderate super-resolution conditions (FWHM = 90 nm) typically afforded by our commercial
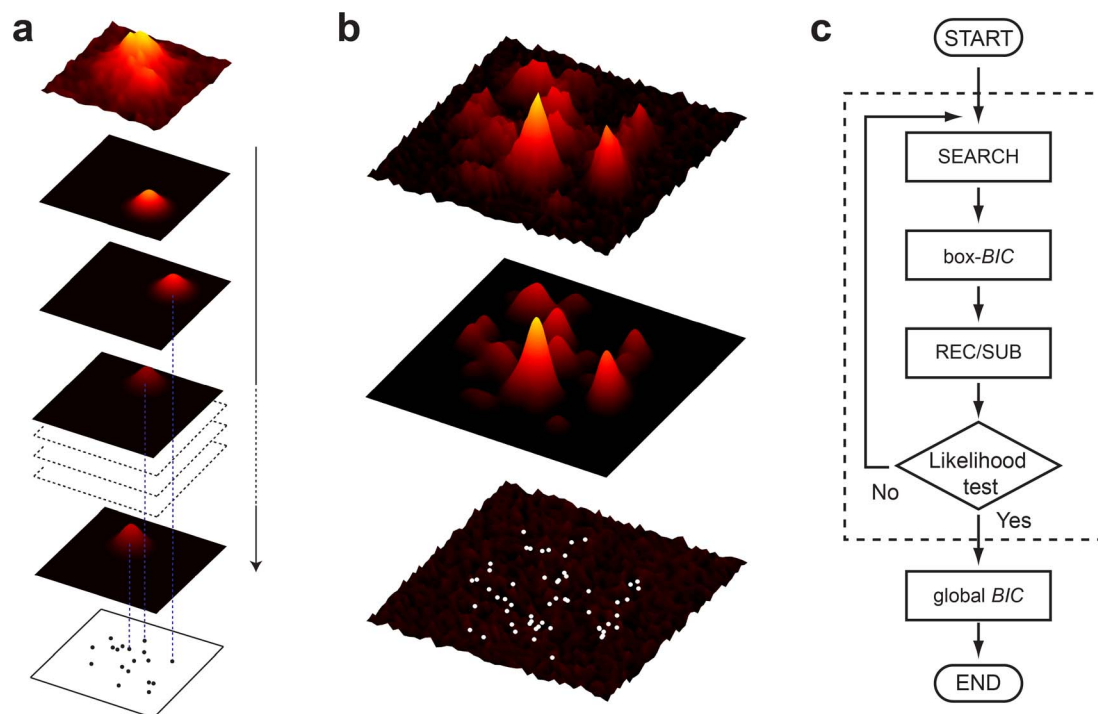
2

Figure 1 | Schematic principle of the algorithm. (a) The nanoscopy image is progressively decomposed into PSFs via BIC analysis, providing the reconstructed image and the molecular localizations of single markers. (b) Representative simulated image showing intensity peaks over a background noise (top) and the reconstructed profile (middle). The bottom panel shows the residual noise and the positions of the localized particles (dots). (c) Flow diagram of the algorithm.

STED microscope[15] and NSOM[13,14]. At densities larger than $\sim$500 μm^{-2} (Fig. 2, lower panels), the finite width of the intensity distribution increases the probability that different molecules separated by distances shorter than the resolution are identified as a single one, affecting the particle localization accuracy and the number of positive detections.

For a quantitative assessment of the algorithm performance, we then calculated the recall fraction R_f, i.e. the ratio between the number of particles correctly identified with localizations and the number of simulated ones[16,17], the localization error L_{err} and the relative intensity error I_{err}. We first evaluated the effect of the instrumental resolution on particle identification and localization (Fig. 3a). Notably, the method yields a high R_f, small L_{err} and I_{err} at receptor densities <200 μm^{-2} for all the investigated resolutions. For densities beyond this value, R_f decays in a resolution-dependent way towards a constant offset ($\sim$0.4), together with a concomitant increase in L_{err} and I_{err}. Notice that for extremely high densities (>1000 μm^{-2}) there is an apparent decrease in L_{err} due to the false identification of closely spaced particles as a single one.

We also evaluated the effect of SNR on the overall performance of the algorithm (Fig. 3b). Changes in SNR (>10 dB) have little impact on R_f and I_{err} and, expectedly, slightly affect L_{err}, which always remains below $\sim$15 nm. At lower SNR (<10 dB), the method loses performance, failing to identify a larger fraction of particles even at low densities. On the other hand, mean (I) and variance (σ_I^2) in the brightness distribution mainly influenced R_f (Fig. 3c–d). The increase of σ_I^2 also affected I_{err} for densities beyond 200 μm^{-2}. This effect is caused by the uncertainty in assigning the exact number of localizations to intense fluorescence spots that, due to a broad intensity distribution, might correspond to one bright marker or several closely located markers. Although molecular clusters can have different shapes, in our simulations we only considered convex molecular arrangements. However, since non-convex shapes can be approximated as sum of convex regions, our conclusions can be extended to different cluster shapes. As a whole, our algorithm

allows reliable analysis of images having resolution, SNR and intensity distribution in a wide range of physiological density settings (<500 μm^{-2}).

Application to STED images of membrane receptors. We next applied our method to investigate the role of different membrane anchors and the cytosolic domain on the nanoscale spatial organization of membrane proteins. Aside from lipid-protein and protein-protein interactions implicated in receptor nanoclustering[1], new evidence indicates that dynamic remodeling of the cortical actin plays a major role on the spatiotemporal organization of cell surface molecules[28]. Indeed, dynamic formation and disassembly of cortical actin might lead to transient concentration fluctuations of lipid anchored proteins (GPI-APs) and nanoclustering of proteins capable of binding directly to actin[28,29]. Therefore, to test how the capacity to bind cortical actin affects nanoscale spatial organization, we acquired STED images of CHO cells stably expressing the GPI-AP folate receptor (FR-GPI), an Ezrin-derived transmembrane variant having an actin filament-binding domain (FRTM-Ez-AFBD) and a mutated version of AFBD unable to bind actin (FRTM-Ez-AFBD*). As an example, typical confocal and STED images of FRTM-Ez-AFBD are shown in Fig. 4a–b, highlighting the increased resolution of STED. To illustrate the ability of the algorithm in recovering molecular positions from individual fluorescence spots on the STED image, regions of the cell have been zoomed-in and shown together with the corresponding reconstructed images and the retrieved localization positions (Fig. 4c). Clearly, a co-existence of monomers and small nanoclusters of the FRTM-Ez-AFBD is observed. The determination of localization positions enables the application of different methods for data quantification, as described below.

Schematic structures of the studied model proteins are depicted in Fig. 5a together with representative STED images and corresponding localizations (Fig. 5b). From the retrieved localizations, the molecular organization was investigated by calculating the nearest-neighbor
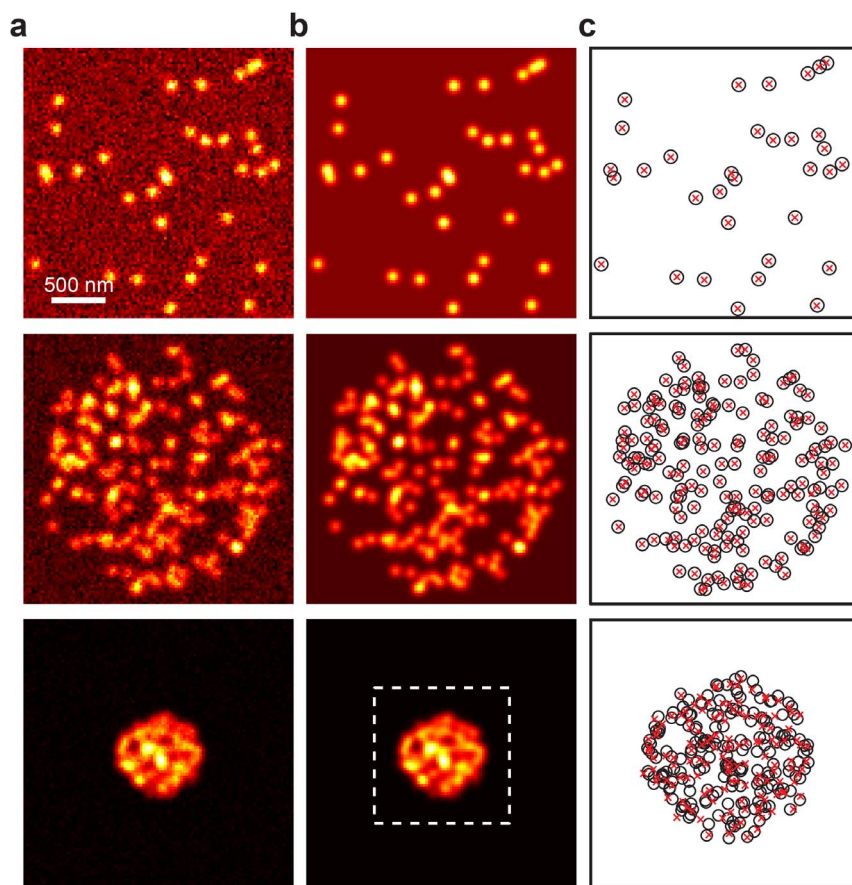
3

Figure 2 | Application of the algorithm to synthetic images with different densities. Simulated images were generated using standard experimental imaging conditions, i.e., resolution = 90 nm, signal-to-noise ratio = 15 dB, average intensity of 100 counts and standard deviation of the intensity of 15 counts. (a) Representative synthetic images at three different densities (5, 50, 500 μm^{-2}, from top to bottom). (b) Corresponding images reconstructed by the PSF decomposition via Bayesian algorithm. (c) Particle localizations retrieved by the algorithm (red crosses) compared with the original particle locations used in the simulations (open circles).

distribution[13] (nnd) and the pair-correlation function[11,12]. Details of the quantification are provided in Supplementary Methods online.

For the FR-GPI, the nnd probability distribution exhibits a sharp peak at a distance of ~50 nm, significantly shorter than the corresponding distribution of randomly organized particles (Fig. 5c). This deviation suggests that a percentage of receptors reside in close proximity, pointing towards the existence of receptor-enriched regions (nanoclusters). To quantify this deviation, we calculated the enhanced proximity probability, defined as the integral of the difference between the observed and simulated nnd. Notably, ~20% of FR-GPI molecules display enhanced proximity, in agreement with previously reported values[13,30].

We further used the pair-correlation function[11,12] to estimate the cluster size and density (Fig. 5e–f). The FR-GPI correlation curves were fitted with an exponential correlation function from which we inferred a nanocluster size of 56 ± 4 nm (mean ± s.d.) with an average of 3.9 ± 0.5 (mean ± s.d.) molecules per nanocluster, consistent with previous observations[12]. Remarkably, the excellent agreement in terms of nanoclustering percentage, size, density and spatial proximal organization of GPI-APs with recently published data[12,13,30] further validates our PSF decomposition approach. Treatment with Latrunculin A (0.5 µM for 10 minutes) to perturb the actin cytoskeleton resulted in a two-fold reduction in the number of molecules per cluster (1.9 ± 0.2) and a corresponding reduction of size (46 ± 4 nm).

The same analyses were also performed over the other two model proteins. For both FRTM-Ez-AFBD and its mutated form FRTM-Ez-AFBD*, the nnd showed a significant deviation from random organization (Fig. 5c, blue and red curves), with a maximum value at ~95 nm, and similar degree of enhancement proximity (~28%). Although this analysis only reveals a twofold increase in the short-distance nnd probability of FRTM-Ez-AFBD with respect to FR-Ez-AFBD*, the homo-FRET measurements in Gowrishankar et al[28] showed that the FRTM-Ez-AFBD molecules form nanoclusters that are tightly packed at the molecular scale (within FRET distances) while FR-Ez-AFBD* does not exhibit a similar arrangement. Similar to the FR-GPI, the pair correlation function for FRTM-Ez-AFBD was well fitted with an exponential correlation function (Fig. 5e, blue curve) rendering a cluster radius of 102 ± 8 nm and an average of 2.9 ± 0.5 molecules per cluster (Fig. 5f). In clear contrast to FR-GPI and FRTM-Ez-AFBD which monotonically approach the value g(r) = 1, FRTM-Ez-AFBD* shows a significant oscillation, dipping at values of g(r) < 1 (anti-correlation) at distances ~200 nm. This indicates that, in contrast to the nanoclusters of FR-GPI and the actin binding protein FRTM-Ez-AFBD, the aggregates of FRTM-Ez-AFBD* are isolated and spaced by a characteristic distance. In order to satisfactorily fit its pair correlation function (Fig. 5e, red curve), we used a damped cosine function, providing a cluster radius of 102 ± 6 nm, an average of 2.0 ± 0.3 molecules per cluster and a characteristic separation distance between nanoclusters of 210 ± 30 nm.

Discussion

With the increasing spread of super-resolution techniques it is becoming highly important the development of automatic methods
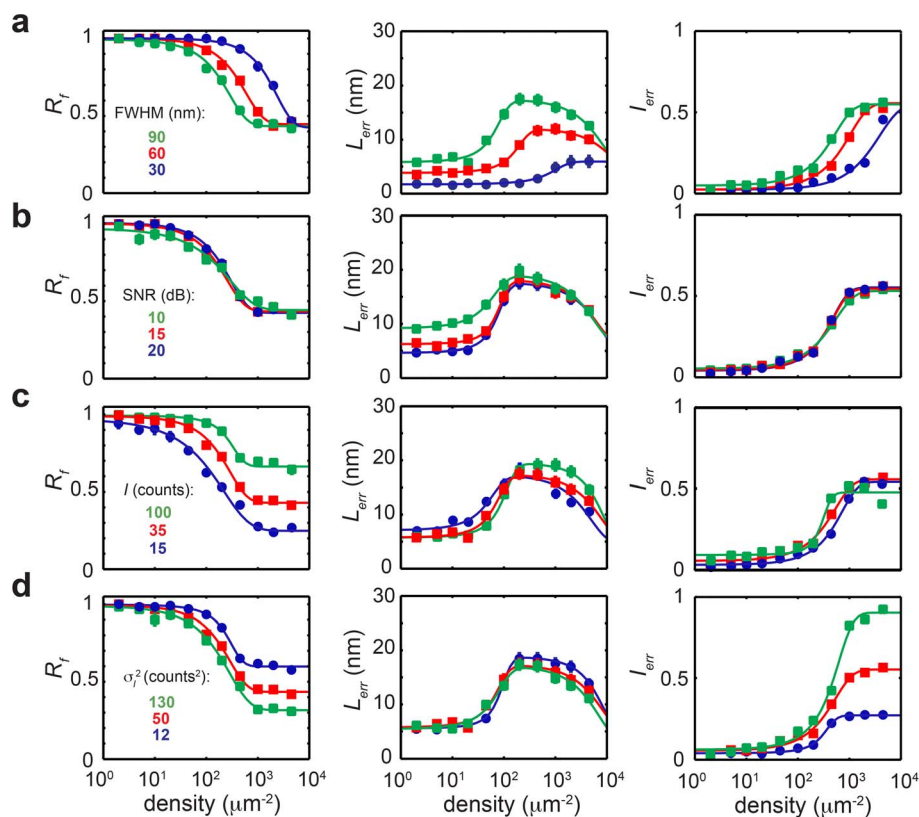
Figure 3 | Quantification of the algorithm performance. The recall fraction R_f, localization error L_{err} and intensity relative error I_{err} were evaluated as a function of molecular density for different experimental settings. (a) For varying image resolution, i.e, FWHM, with SNR = 15 dB, I = 35 counts, $\sigma_I^2 = 50$ counts^2. (b) For varying SNR, with FWHM = 90 nm, I = 35 counts, $\sigma_I^2 = 50$ counts^2. (c) For varying mean intensity value I, with FWHM = 90 nm, SNR = 15 dB, $\sigma_I^2 = 50$ counts^2 and (d) for varying width of the intensity distribution σ_I^2, with FWHM = 90 nm, SNR = 15 dB and I = 35 counts.

capable of extracting unbiased quantitative information from nanoscopy images. Here we described an algorithm that allows determination of molecular localizations from dense images, enabling quantification of receptor organization from super-resolution techniques such as STED and NSOM. The method provides a solution to the automated analysis of images generated by these techniques and increases their powerfulness by adding the possibility to extract molecular localizations from highly dense aggregates. In comparison

to other algorithms that can also deal with overlapping PSFs[16–18,20–23], our method combines a sub-region selection routine within a deflation loop which hierarchically defines the areas of the image were the analysis is performed. Besides saving computational time, this approach is crucial for the precise reconstruction of dense clusters. A second advantage is provided by the implementation of the likelihood analysis for marker brightness based on the experimental intensity distribution. This analysis allows faithful extraction of the
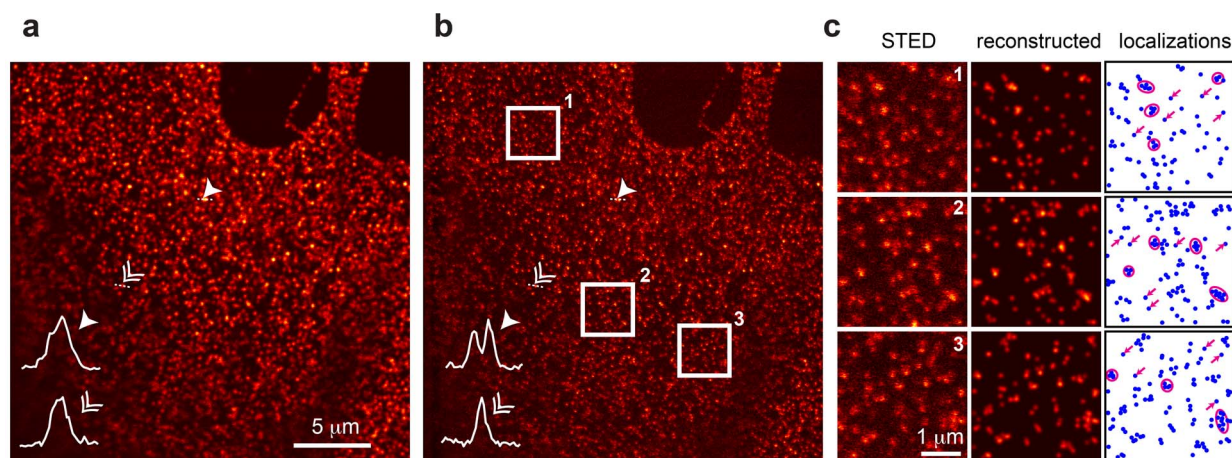

Figure 4 | Application of the algorithm to STED images. (a–b) Confocal (a) and STED (b) image of a CHO cell stably transfected with FRTM-Ez-AFBD. Intensity profiles of selected features (arrowheads) show the increased resolution obtained with STED as compared to confocal microscopy. STED resolution was evaluated from images of isolated markers under the same imaging conditions, giving a FWHM = 93 ± 15 nm (s.d.). (c) Zoomed-in regions corresponding to the squared areas in (b), together with the corresponding reconstructed images and localization maps. In the localization maps, arrows indicate isolated receptors whereas ellipses encircle representative nanoclusters appearing as intense spots in the STED image.
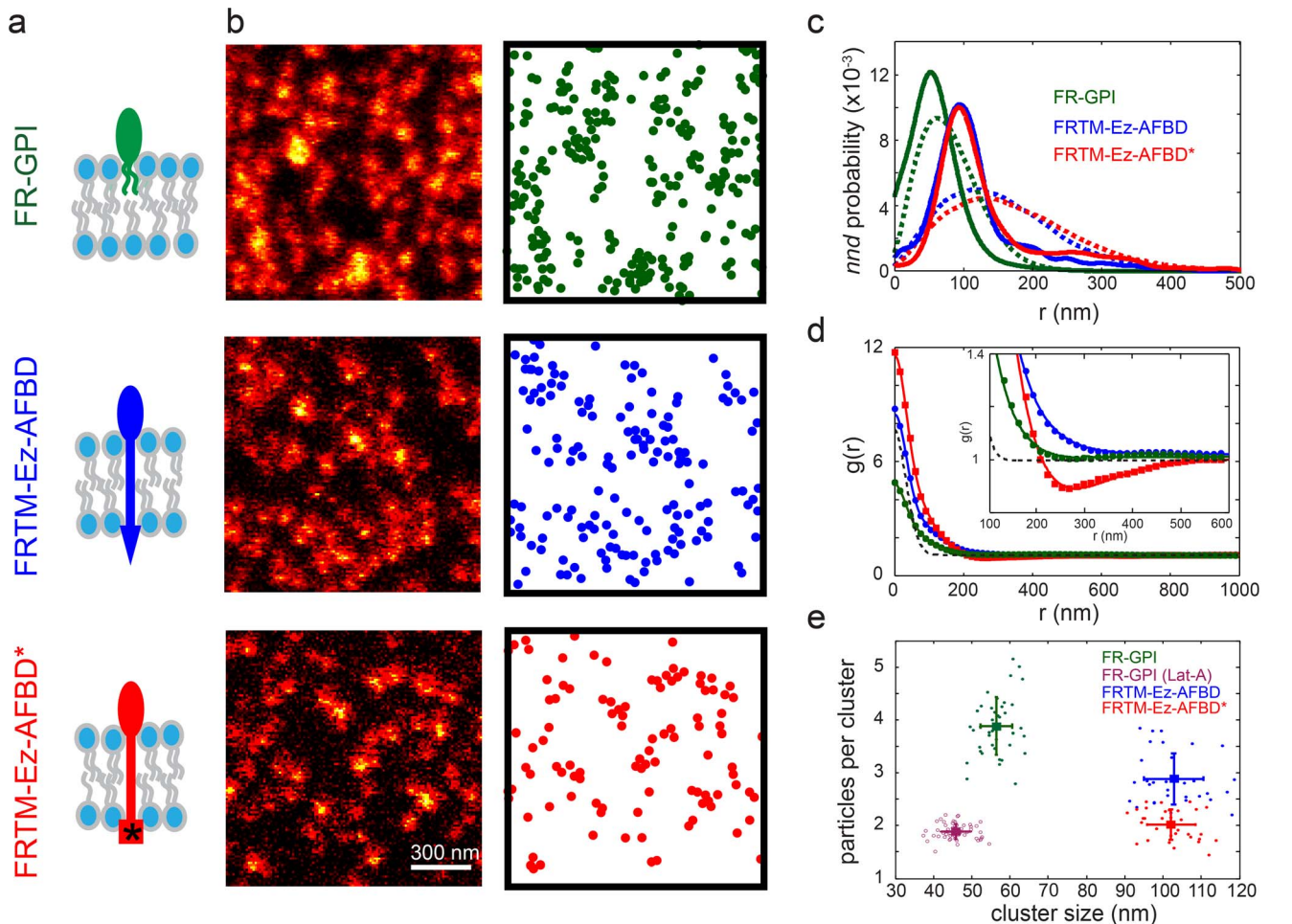
Figure 5 | Quantification of molecular organization of membrane receptors having different membrane anchors and cytoplasmic features. (a) Schematic representation of the model receptors. (b) Representative STED images of CHO cells expressing the three model proteins and corresponding localizations maps. The average localization accuracy is ~25 nm. The localizations obtained for several cells (at least three for each receptor) were used to quantify the data. (c) nnd distributions (continuous lines) for the FR-GPI (green), FRTM-Ez-AFBD (blue) and FRTM-Ez-ABFD* (red) compared to the nnd distributions obtained from simulations of random organization at the corresponding experimental molecular densities (dashed curves) (d) Pair correlation function g(r) for the three proteins investigated. The first part of the curves (<100 nm) shows a Gaussian decay, which accounts for the average localization error with an amplitude inversely proportional to the average molecular density (ρ = 43, 18 and 11 μm^{-2} for FR-GPI, FRTM-Ez-AFBD and FRTM-Ez-ABFD*, respectively). For distances larger than ~100 nm, a slower decay is observed (zoom-in region in the inset) reflecting the non-random molecular organization of the three proteins. The dashed line corresponds to the pair correlation function of uncorrelated (random) receptor organization, with ρ = 23 μm^{-2} and a localization accuracy of 25 nm. (e) Scatter plot of the number of particles per cluster versus cluster size obtained by pair-correlation analysis on several cellular regions. Error bars correspond to standard deviation.

number of markers from overlapping PSFs, thus providing better estimation of cluster stoichiometry and limiting the number of missed events even at high molecular densities. Based on analysis of synthetic images, we estimated up to a five-fold increase in the density at which 50% of the localizations are correctly retrieved compared to other algorithms[22] (see Supplementary Fig. S3). However, such values strongly depend on the fluorescent marker used and the associated brightness distribution, as high variance in fluorophores emission reduces the advantages of the Bayesian analysis of intensity (Fig. 3). Therefore, accurate image quantification requires proper choice of fluorescent markers and fluorophore-per-antibody stoichiometry. We point out that the retrieved localizations reflect the positions of the labeling marker and, as such, the use of large markers might produce inaccuracies in assessing the positions of the labeled receptor molecules. In addition, steric hindrance might limit exact stoichiometry quantification. The computational effort of the algorithm depends on image size and marker density. For the analysis of a region of 128 $\times$ 128 pixels^2 containing ~2000 markers, processing on a single core i7 (3.40 GHz) requires ~30 minutes. To

reduce computational time, large images can be analyzed by breaking them down into a number of small areas or, alternatively, by using Graphic Processing Unit architecture[18,31] or cluster computers.

The application of our algorithm to STED images enabled quantification of membrane protein spatial organization. By investigating proteins with different membrane anchors and cytosolic domains, our analysis revealed the subtle role of the cortical actin on the membrane architecture. In the cases of the lipid-tethered protein and the transmembrane protein with an actin-binding motif, interaction with short dynamic actin coupled to motor activity might create sites for local concentration of these molecules (asters)[28]. In this context, the similarity between FRTM-Ez-AFBD and FR-GPI, both showing comparable organization as well as the effect of Lat-A on FR-GPI organization, point towards an indirect influence of actin on the lipid anchor, either via coupling to actin-binding proteins or via lipid-based transbilayer interactions[28,29]. In addition, the actin meshwork could also work as a scaffold to induce nanoclusters, facilitating the formation of larger platforms. In the case of the FRTM-Ez-AFBD*, the agreement between r_0 and the characteristic
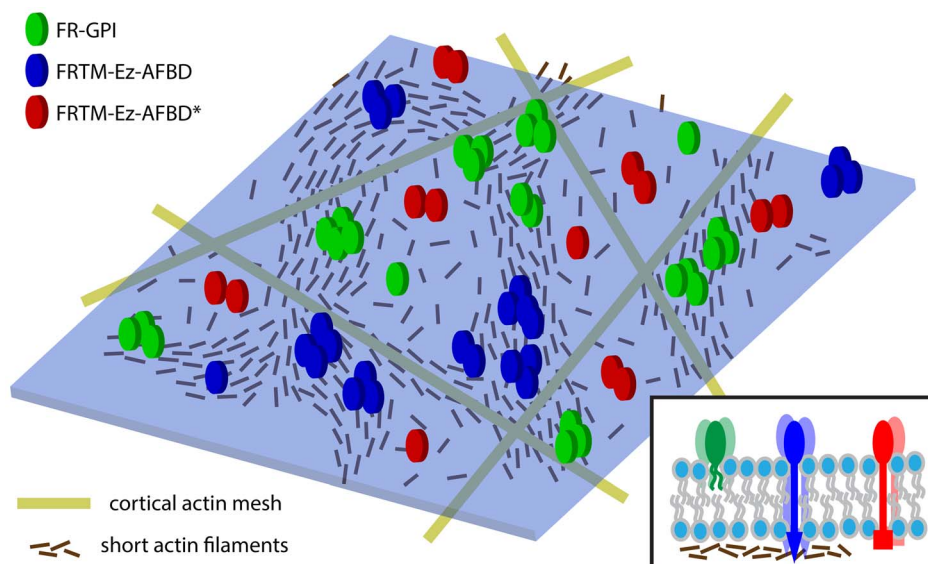
Figure 6 | Schematic model of the effect of actin on membrane receptor organization. Interaction of the lipid-tethered protein (FR-GPI) and the actin-binding transmembrane protein (FRTM-Ez-AFBD) with the actin cytoskeleton, via lipid-based transbilayer interactions or by direct actin binding, induces the formation of large receptor platforms. The lack of this interaction in the mutated receptor (FRTM-Ez-AFBD*) prevents large-scale correlation and confines the receptors within the actin meshwork.

size of the cytoskeletal meshwork[32] indicates that the actin network might act in here as a barrier, not only by reducing FRTM-Ez-AFBD* aggregation but also by keeping the clusters away from each other (Fig. 6).

Although the method has been applied for the analysis of receptor heterogeneity on the cell membrane, its applications can readily include the study of *a priori* unknown dense subcellular structures and compartments.

Methods

SI Methods provides a detailed description of the algorithm and further details on the quantification of receptors spatial organization.

Cell culture. Chinese hamster Ovary (CHO) cell lines expressing folate receptor (FR) constructs were maintained in folate-free HF12 medium (Himedia Labs) supplemented with 10% FBS (Gibco), 1% Pen/Strep/Glut (PAA), 200 μg/ml geneticin and 100 μg/ml hygromycin (both from Invitrogen) as described in an earlier publication[33]. CHO cells expressing GPI-anchored folate receptor (FR-GPI) were obtained as previously described[33]. The transmembrane fusion proteins, FRTM-Ez-AFBD and FRTM-Ez-AFBD* (R579A mutant), both encoding an actin-filament-binding domain (AFBD) protein were generated from FRTM[34] as previously described[28].

Receptors labeling. Labeling experiments were performed typically in 35 mm coverslip dishes (Fluorodish, World Precision Instruments), 36–48 hr after plating under cell culture conditions. Cells were washed in a HEPES-based medium (M1, pH 7.4) containing 150 mM NaCl, 5 mM KCl, 1 mM CaCl$_2$, 1 mM MgCl$_2$ and 20 mM HEPES (all purchased from Sigma). Next, the cells were fixed in a 2% PFA containing M1 solution for 30 min. Blocking was assured by incubating the fixed sample with 3% BSA and 1 mM Glycine containing M1 for 20 min. Subsequently, the folate fusion proteins were labeled by incubating the sample for 30 min with 5 μg/ml of the anti-folate receptor monoclonal Mov18 (Enzo life sciences) in M1. Fluorescent labeling was subsequently obtained through the incubation of the sample with 5 μg/ml GαM secondary antibody conjugated with Alexa 488 (Invitrogen) in M1 for 30 min. Samples were thoroughly washed with M1 between each of the fixation and labeling steps. The STED measurements were performed directly after labeling. Actin perturbation was performed by incubating the cells 10 min at 37°C with 0.5 μM Latrunculin A before the fixation step.

Simulations and algorithm performance evaluation. To evaluate the performance of the algorithm, we analyzed synthetic images generated by randomly positioning fluorescent emitters in confined areas. The simulated positions were convoluted with bi-dimensional Gaussian distributions whose peak intensities were randomly selected from a normal emitter distribution with mean I and variance σ_I^2. According to the Nyquist theorem for diagonal sampling, the images were pixelated at 3.5–4 pixels per FWHM and, after the addition of fixed background intensity, corrupted with Poisson noise. To check the reliability of the method in different experimental conditions, simulations were performed at several molecular densities by varying the FWHM, the signal-to-noise ratio $\left(SNR = 20\log_{10}\left(\frac{I}{\sigma_{bkg}}\right)\right)$, as well as the average and the width of the marker intensity distribution.

The algorithm performance was evaluated by calculating the recall fraction, the localization error and the relative intensity error. The recall fraction, i.e. the ratio between the number of localized markers and the number of simulated ones, was calculated as previously described[16,17]. The localization error was calculated as the root-mean-square distance between a localization and the simulated position[16]. Similarly, the relative intensity error was calculated as the root-mean-square intensity difference divided by the average intensity. The percentage of false positive identification was found to be <4% for all the investigated conditions.

STED nanoscopy. STED images were obtained with a commercial Leica STED setup (TCS-SP5; Leica) equipped with a 100× 1.4NA oil objective (HCX PL APO CS, Leica) and galvo scanner mirrors set to resonate at 8 kHz. Alexa 488 fluorophores were excited using the 488-nm ArKr laser line at 5% (~1 μW). The fluorescence was detected after passing a 1 airy pinhole (151.5 μm) and optical filters permeable for light of wavelengths between 490 and 585 nm with a photomultiplier tube set at a gain of 467.1 V. To obtain maximum optical resolution the 592 nm STED depletion beam was set at 100% (~100 mW). Line accumulation was set at 8 and each image was averaged over 16 frames. Image acquisition was set at 1024 × 1024 pixels with 12-bit pixel depth.

The alignment of the two beams (excitation and STED) was performed automatically and accepted only when it required little displacement voltages. The alignment was regularly checked for drift after each measurement. The optical resolution was assessed before each experiment by imaging the size distribution of 20 nm beads and typically was 90–100 nm. Images of Alexa 488 conjugated secondary antibodies were also obtained to quantify optical resolution and marker intensity distribution (see Supplementary Fig. S1). In order to quantitatively compare the organization of the different constructs, we used identical image acquisition settings in all cases.

Quantification of receptors spatial organization. Receptor spatial organization was quantified by calculating the nnd[13] and the pair-correlation function[11,12], from the localization coordinates obtained via application of the algorithm to the STED images and taking into account the related localization accuracy. Details of the calculations are provided in SI Methods.

1. Bethani, I., Skanland, S. S., Dikic, I. & Acker-Palmer, A. Spatial organization of transmembrane receptor signalling. *EMBO J.* **29**, 2677–2688 (2010).
2. Manz, B. N. & Groves, J. T. Spatial organization and signal transduction at intercellular junctions. *Nat. Rev. Mol. Cell Biol.* **11**, 342–352 (2010).
3. Kusumi, A. *et al.* Dynamic organizing principles of the plasma membrane that regulate signal transduction: commemorating the fortieth anniversary of Singer and Nicolson's fluid-mosaic model. *Annu. Rev. Cell Dev. Biol.* **28**, 215–250 (2012).
4. Rust, M. J., Bates, M. & Zhuang, X. W. Sub-diffraction-limit imaging by stochastic optical reconstruction microscopy (STORM). *Nat. Methods* **3**, 793–795 (2006).
5. Betzig, E. *et al.* Imaging intracellular fluorescent proteins at nanometer resolution. *Science* **313**, 1642–1645 (2006).

6. Hess, S. T., Girirajan, T. P. K. & Mason, M. D. Ultra-high resolution imaging by fluorescence photoactivation localization microscopy. *Biophys. J.* **91**, 4258–4272 (2006).

7. Hell, S. W. & Wichmann, J. Breaking the Diffraction Resolution Limit by Stimulated-Emission - Stimulated-Emission-Depletion Fluorescence Microscopy. *Opt. Lett.* **19**, 780–782 (1994).

8. Klar, T. A., Jakobs, S., Dyba, M., Egner, A. & Hell, S. W. Fluorescence microscopy with diffraction resolution barrier broken by stimulated emission. *Proc. Natl. Acad. Sci. U. S. A.* **97**, 8206–8210 (2000).

9. de Lange, F. *et al.* Cell biology beyond the diffraction limit: near-field scanning optical microscopy. *J. Cell Sci.* **114**, 4153–4160 (2001).

10. Hess, S. T. *et al.* Dynamic clustered distribution of hemagglutinin resolved at 40 nm in living cell membranes discriminates between raft theories. *Proc. Natl. Acad. Sci. U. S. A.* **104**, 17370–17375 (2007).

11. Veatch, S. L. *et al.* Correlation functions quantify super-resolution images and estimate apparent clustering due to over-counting. *PLoS ONE* **7**, (2012).

12. Sengupta, P. *et al.* Probing protein heterogeneity in the plasma membrane using PALM and pair correlation analysis. *Nat. Methods* **8**, 969–975 (2011).

13. van Zanten, T. S. *et al.* Hotspots of GPI-anchored proteins and integrin nanoclusters function as nucleation sites for cell adhesion. *Proc. Natl. Acad. Sci. U. S. A.* **106**, 18557–18562 (2009).

14. van Zanten, T. S. *et al.* Direct mapping of nanoscale compositional connectivity on intact cell membranes. *Proc. Natl. Acad. Sci. U. S. A.* **107**, 15437–15442 (2010).

15. Manzo, C. *et al.* The neck region of the C-type lectin DC-SIGN regulates its surface spatiotemporal organization and virus-binding capacity on antigen-presenting cells. *J. Biol. Chem.* **287**, 38946–38955 (2012).

16. Holden, S. J., Uphoff, S. & Kapanidis, A. N. DAOSTORM: an algorithm for high-density super-resolution microscopy. *Nat. Methods* **8**, 279–280 (2011).

17. Wolter, S. *et al.* Real-time computation of subdiffraction-resolution fluorescence images. *J. Microsc.* **237**, 12–22 (2010).

18. Huang, F., Schwartz, S. L., Byars, J. M. & Lidke, K. A. Simultaneous multiple-emitter fitting for single molecule super-resolution imaging. *Biomed. Opt. Express* **2**, 1377–1393 (2011).

19. Mortensen, K. I., Churchman, L. S., Spudich, J. A. & Flyvbjerg, H. Optimized localization analysis for single-molecule tracking and super-resolution microscopy. *Nat. Methods* **7**, 377–U359 (2010).

20. Quan, T. W. *et al.* High-density localization of active molecules using Structured Sparse Model and Bayesian Information Criterion. *Opt. Express* **19**, 16963–16974 (2011).

21. Mukamel, E. A., Babcock, H. & Zhuang, X. W. Statistical deconvolution for superresolution fluorescence microscopy. *Biophys. J.* **102**, 2391–2400 (2012).

22. Zhu, L., Zhang, W., Elnatan, D. & Huang, B. Faster STORM using compressed sensing. *Nat. Methods* **9**, 721–723 (2012).

23. Babcock, H. P., Moffitt, J. R., Cao, Y. & Zhuang, X. Fast compressed sensing analysis for super-resolution imaging using L1-homotopy. *Opt. Express* **21**, 28583–28596 (2013).

24. Zhang, B., Zerubia, J. & Olivo-Marin, J. C. Gaussian approximations of fluorescence microscope point-spread function models. *Appl. Opt.* **46**, 1819–1829 (2007).

25. Burnham, K. P. & Anderson, D. R. *Model Selection and Multi-Model Inference: A Practical Information-Theoretic Approach.* (Springer, 2002).

26. Serge, A., Bertaux, N., Rigneault, H. & Marguet, D. Dynamic multiple-target tracing to probe spatiotemporal cartography of cell membranes. *Nat. Methods* **5**, 687–694 (2008).

27. de Bakker, B. I. *et al.* Nanoscale organization of the pathogen receptor DC-SIGN mapped by single-molecule high-resolution fluorescence microscopy. *Chemphyschem* **8**, 1473–1480 (2007).

28. Gowrishankar, K. *et al.* Active remodeling of cortical actin regulates spatiotemporal organization of cell surface molecules. *Cell* **149**, 1353–1367 (2012).

29. Goswami, D. *et al.* Nanoclusters of GPI-anchored proteins are formed by cortical actin-driven activity. *Cell* **135**, 1085–1097 (2008).

30. Sharma, P. *et al.* Nanoscale organization of multiple GPI-anchored proteins in living cell membranes. *Cell* **116**, 577–589 (2004).

31. Smith, C. S., Joseph, N., Rieger, B. & Lidke, K. A. Fast, single-molecule localization that achieves theoretically minimum uncertainty. *Nat. Methods* **7**, 373–375 (2010).

32. Morone, N. *et al.* Three-dimensional reconstruction of the membrane skeleton at the plasma membrane interface by electron tomography. *J. Cell Biol.* **174**, 851–862 (2006).

33. Mayor, S. & Maxfield, F. R. Insolubility and redistribution of GPI-anchored proteins at the cell-surface after detergent treatment. *Mol. Biol. Cell* **6**, 929–944 (1995).

34. Varma, R. & Mayor, S. GPI-anchored proteins are organized in submicron domains at the cell surface. *Nature* **394**, 798–801 (1998).

Acknowledgments

Author contributions

C.M. devised the method and performed the analysis. T.S.vZ., S.S and J.A.T.-P. carried out experiments. C.M. and M.F.G.-P. wrote the manuscript. S.M. and M.F.G.-P. supervised research. All authors reviewed the manuscript.

Additional information